9

Convective Instability in Complex Fluids

So far we have assumed that the equation of state is trivial: buoyancy is proportional to a single fluid property (e.g., temperature) that varies only due to advection and diffusion (section 1.5). Real geophysical fluids may be much more complicated than this. For example, buoyancy may be controlled by two or more scalar constituents with different chemical properties, or by phase changes (e.g., freezing). The equation of state may include nonlinearities; for example, a mixture of two constituents may be lighter or denser than either constituent individually. The scalars that control buoyancy may have complex properties such as being alive. All of these properties affect the stability of the fluid. In this chapter we consider a few simple examples in which buoyancy changes lead to convection.

9.1 Conditional Instability in a Moist Atmosphere or a Freezing Ocean

Instability may result when the fluid undergoes a phase change. For example, atmospheric motions may be greatly affected by humidity. Humidity is in some ways an analog of salinity in the ocean but, unlike salt, water in the atmosphere can exist in liquid, solid, and gas phases. Changes between these phases affect the temperature of the air, and therefore its buoyancy.

If the pressure in an air parcel drops, so does its capacity to hold water vapor in the gas state. If the humidity is close to its saturation value, pressure reduction causes water vapor to condense to the liquid state, releasing latent heat into the air (and creating rain). A rising air parcel, if moist enough, will be warmed by condensation and therefore rise even faster. This is called *conditional* instability, as it depends not only on the vertical temperature gradient but also on the humidity. In a falling air parcel, rising pressure increases the air's capacity to hold water vapor, allowing liquid water to evaporate, but any liquid water present is likely to precipitate as rain before this can happen.

222

Figure 9.1 Two convective phenomena visible from Kume Island, near Japan. In the foreground, lava has cooled from above, forming hexagonal and pentagonal cells (cf. section 2.5). In the distance, cumulus clouds are driven by conditional convective instability (section 9.1). Credit: Ippei Naoi/ Moment/ Getty Images

Conditional instability is quantified in terms of a *saturated* (or *moist*) adiabatic lapse rate Γ_s, whereas the quantity defined in section 2.7 as Γ is actually the *dry* adiabatic lapse rate, henceforth called Γ_d. Γ_s varies considerably with temperature and pressure but is always less than Γ_d; a typical value is 6°C/km. Saturated air can therefore be in one of three states depending on the measured lapse rate $\Gamma = -\partial T/\partial z$:

  (i) $\Gamma < \Gamma_s$, stable,
 (ii) $\Gamma_s < \Gamma < \Gamma_d$, conditionally unstable,
(iii) $\Gamma > \Gamma_d$, unstable.

Conditional instability is often responsible for the formation of cumulus clouds (e.g., Figure 9.1; note rain on horizon at left).

An interesting variant of conditional instability has been observed in the polar oceans (Foldvik and Kvinge, 1974; Jordan et al., 2015). The process depends on the formation of tiny ice crystals called *frazil*, which happens when water is supercooled (cooled below its freezing point but not yet frozen). A parcel of supercooled water can be thought of as a mixture of liquid water and frazil. As the frazil content increases, the parcel becomes less dense (since ice is lighter than water), and therefore rises. The resulting pressure drop increases the freezing point of water, so that the water is increasingly supercooled and frazil formation is accelerated.

9.2 Double Diffusive Instabilities

9.2.1 Some History

The class of processes known as double diffusion operates in a wide range of fluid environments, from the Earth's mantle to stellar interiors (Schmitt, 1983). It depends on two conditions: (i) that the buoyancy is a function of two different scalars (hence the "double"), and (ii) that they diffuse at different rates (hence "diffusion"). In the oceanographic context the scalars are temperature and salinity, and salt diffuses much more slowly than heat.

The discovery of double diffusion has an interesting history. In the nineteenth century, Jevons (1857) conducted an experiment similar to that shown in Figure 9.2. He produced the structures we now recognize as salt fingers, though he was not able to explain them. Later in 1880, the formidable Lord Rayleigh reproduced Jevons' experiment, but even he was unable to deduce the mechanism. The oceanographer Vagn Walfrid Ekman (Ekman, 1906) studied internal waves by means of a layer of milk laid carefully over a layer of salt water. He observed a shower of small vortex rings. While he recognized the role of molecular diffusion in this phenomenon, he did not realize that it would happen naturally in the ocean.

An important step forward was made when a group of oceanographers (Stommel et al., 1956) were discussing how to measure pressure changes in the tropical Atlantic Ocean using a pipe that would be inserted vertically into the water column. They realized that, if the water in the pipe was displaced upwards, it would continue to flow indefinitely (Figure 9.3). Their reasoning rested on the fact that the ocean is saltiest at the surface in that region due to evaporation. The buoyancy distribution is nevertheless stable because the surface waters are warmer (Figure 9.3, profiles at left). Water entering at the bottom of the pipe is therefore relatively cool and fresh, but as it rises, it is surrounded by warmer water and is therefore warmed by the

Figure 9.2 Laboratory experiment showing the formation of salt fingers. Assistance with the experiment provided by Christoph Funke.
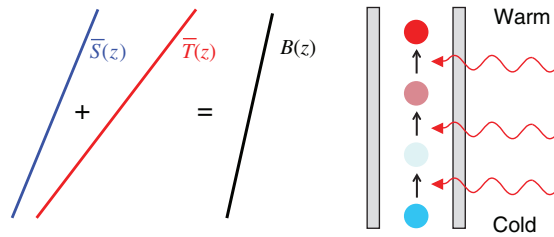
Figure 9.3 Schematic of the perpetual salt fountain, which is analogous to the growth of salt fingers when warm salty water overlies cooler, fresher water. If the water in the pipe is displaced upward, each fluid parcel moves into a warmer environment and therefore absorbs heat. It does not absorb salt, however, because the wall of the pipe prevents it. Since the water is now fresher (and thus lighter) than its surroundings, it continues to rise. Because the diffusivity of salt is negligible, the process works even without the pipe.

heat flux through the pipe. Unlike heat, salt cannot pass through the pipe, the result being that the enclosed water remains fresher, and therefore more buoyant, than its surroundings. Their now-classic paper is called "An Oceanographic Curiosity: the Perpetual Salt Fountain."

Stommel's colleague Melvin Stern soon realized that the salt fountain is more than a "curiosity" – because salt diffuses much more slowly than heat, Stommel's pipe is not actually needed! The phenomenon should occur naturally wherever warm, salty water overlays cool fresh water (Stern, 1960). We now know that this is true, and the pipeless salt fountains are called salt fingers.

9.2.2 Parameters Describing Thermohaline Stratification

When changes in density are caused by only small variations in temperature T and salinity S from reference values T_0, S_0, we use the linearized equation of state (reproducing 1.23):[1]

$$b(T, S) = g\alpha(T - T_0) - g\beta(S - S_0), \qquad (9.1)$$

where α and β are constants evaluated at $T = T_0, S = S_0$. Denoting the background profiles of T and S with overbars, the background vertical buoyancy gradient is then

$$B_z = g\alpha\bar{T}_z - g\beta\bar{S}_z. \qquad (9.2)$$

A useful and easily measured parameter for characterizing compound stratification is (minus) the ratio of thermal and saline contributions to B_z:

---

[1] More generally, the equation of state for seawater is also a function of pressure. It is determined very precisely using a 48-term polynomial equation(!), and can also involve other variables such as sediment concentration or dissolved gases.

$$R_\rho = \frac{\alpha \bar{T}_z}{\beta \bar{S}_z}.$$

The individual components of B_z can be written as

$$g\alpha \bar{T}_z = \frac{B_z R_\rho}{R_\rho - 1}, \qquad \text{and} \quad g\beta \bar{S}_z = \frac{B_z}{R_\rho - 1}. \tag{9.3}$$

We will only consider the situation where $R_\rho > 0$ and $B_z > 0$. In this case $g\alpha \bar{T}_z$ and $g\beta \bar{S}_z$ have the same sign, i.e., one makes a positive contribution to B_z while the other makes a (smaller) negative contribution. It is in this situation that double diffusive instabilities may occur. The case in which $g\alpha \bar{T}_z$ and $g\beta \bar{S}_z$ are both positive is sketched in Figure 9.3.

An important special case is that of compensating temperature and salinity. If $R_\rho = 1$, then the thermal and saline contributions to the buoyancy gradient cancel each other out. The mean density profile is then uniform despite the variations in temperature and salinity.[2]

Other useful parameters include

- the Prandtl number $Pr = \nu/\kappa_T$,
- the Schmidt number $Sc = \nu/\kappa_S$ and
- the diffusivity ratio $\tau = \kappa_S/\kappa_T$.

9.2.3 Perturbation Equations

By substituting $b = B(z) + \epsilon b'$, $T = \bar{T}(z) + \epsilon T'$, and $S = \bar{S}(z) + \epsilon S'$ into (9.1), we obtain the buoyancy perturbation

$$b' = g\alpha T' - g\beta S'.$$

This is substituted into the perturbation equation for a motionless stratified equilibrium (2.17) to give

$$\frac{\partial}{\partial t} \nabla^2 w' = g\alpha \nabla_H^2 T' - g\beta \nabla_H^2 S' + \nu \nabla^4 w'. \tag{9.4}$$

Equations for the temperature and salinity perturbations are obtained by substituting the perturbation solutions into (1.24) and linearizing:

$$\frac{\partial}{\partial t} T' = -\bar{T}_z w' + \kappa_T \nabla^2 T', \tag{9.5}$$

---

[2] It is well known that the ocean tends to arrange itself into more-or-less horizontal layers that are homogeneous in density. But because of this compensation property, those layers are not necessarily homogeneous in temperature or salinity. This can lead to *thermohaline interleaving* as discussed in section 12.2.2.

$$\frac{\partial}{\partial t} S' = -\bar{S}_z \, w' + \kappa_S \nabla^2 S'. \tag{9.6}$$

We have assumed, as for the previous case of pure convection, that the profiles of $\bar{T}(z)$ and $\bar{S}(z)$ are linear (see section 2.1.1), i.e., $\bar{T}_z$ and $\bar{S}_z$ are both constants, so that there is no change in time of the background profiles due to diffusion.

Assuming that each of the three unknowns w', T', S' has the usual normal mode form, e.g., $w' = W_r$ where

$$W \sim e^{\sigma t + \iota(kx + \ell y + mz)},$$

we can derive an algebraic equation for σ:

$$(\sigma + \nu K^2)(\sigma + \kappa_T K^2)(\sigma + \kappa_S K^2) + (\sigma + \kappa_S K^2)\frac{C^2 B_z R_\rho}{R_\rho - 1} - (\sigma + \kappa_T K^2)\frac{C^2 B_z}{R_\rho - 1} = 0, \tag{9.7}$$

where $C = \tilde{k}/K$ is the cosine of the angle of elevation (Figure 2.2).[3] Collecting powers of σ, we write (9.7) as a cubic polynomial equation

$$\sigma^3 + A_2 \sigma^2 + A_1 \sigma + A_0 = 0 \tag{9.8}$$

with coefficients

$$A_2 = (Pr + 1 + \tau)\kappa_T K^2$$
$$A_1 = (Pr + Pr\tau + \tau)\kappa_T^2 K^4 + C^2 B_z$$
$$A_0 = Pr \, \tau \kappa_T^3 K^6 + C^2 B_z \kappa_T \frac{\tau R_\rho - 1}{R_\rho - 1} \, K^2.$$

While (9.8) is cubic and is therefore awkward to solve analytically, it has some simplifying properties that allow us to identify regions of parameter space where different types of instability are found. First, the coefficients of (9.8) are real. Second, A_1 and A_2 are positive definite, provided only that $B_z > 0$ and $K \neq 0$. Only A_0 can take either sign. Using these properties, one may deduce that

- stationary instability exists when $A_0 < 0$, and
- oscillatory instability exists when $A_0 > A_1 A_2$.

If you enjoy this sort of thing, you may wish to complete project B.5 (appendix B), in which these regions are identified.

The requirement $A_0 < 0$ for stationary instability is fulfilled (at least for some range of K) provided that the second term in A_0 is negative, or

$$1 < R_\rho < \frac{1}{\tau}. \tag{9.9}$$

---

[3] Exercise: Eliminate salinity from (9.7) by taking $\kappa_S = 0$ and $R_\rho \to \infty$. Compare the result with (2.45). Now eliminate temperature by setting $\kappa_T = 0$ and $R_\rho = 0$ and compare again.

Similarly (albeit with more algebra), we can show that the requirement $A_0 > A_1 A_2$ for oscillatory instability is equivalent to

$$\frac{Pr + \tau}{Pr + 1} < R_\rho < 1. \tag{9.10}$$

For seawater, with $Pr = 7$ and $\tau = 0.01$, these ranges become $1 < R_\rho < 100$ for stationary modes and $0.876 < R_\rho < 1$ for oscillatory modes. As R_ρ is increased past unity, the fastest-growing instability changes from oscillatory to stationary (Figure 9.4a). Both mode types grow fastest when R_ρ is near 1, where the net stratification is weakest. The two classes of unstable modes represent distinctly different physical processes, as we describe in the upcoming subsections.

9.2.4 Salt Finger Instability

In the first instance, we will examine the basic state profiles shown in Figure 9.3, where both $\bar{T}$ and $\bar{S}$ increase with height, z. This is called the salt-finger, or just *finger regime*, for reasons that we will soon see. In this regime, $R_\rho > 1$. While salt fingering instability is mathematically possible for R_ρ as high as $\tau^{-1} \sim 100$, the phenomenon is usually observed when R_ρ is ~ 2 or less. Salt fingering instability
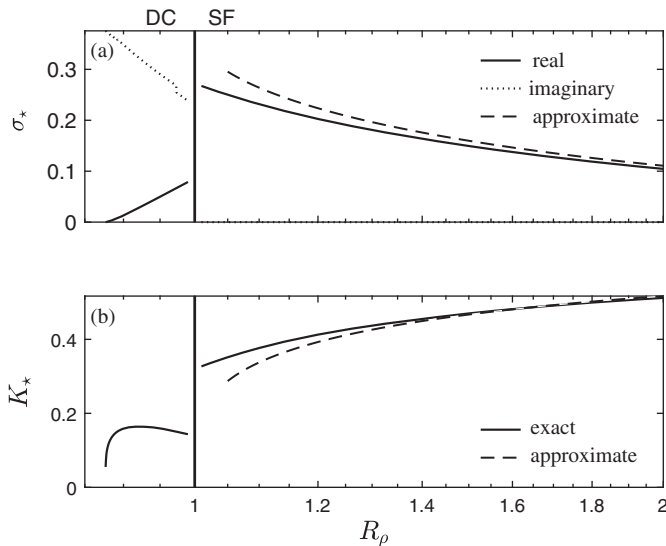

Figure 9.4 Growth rate (a; scaled by $|g\alpha T_z|^{1/2}$) and wavenumber (b; scaled by $[|g\alpha T_z|/\kappa_T^2]^{1/4}$) for double diffusive instability as described by (9.8). Results pertain to the fastest-growing instability at each R_ρ. $R_\rho > 1$: stationary salt fingering modes (section 9.2.4); $R_\rho < 1$: oscillatory diffusive convection (section 9.2.5). The Prandtl number and diffusivity ratio are set to $Pr = 7$ and $\tau = 0.01$, typical values for seawater. Dashed curves indicate the approximation (9.11).
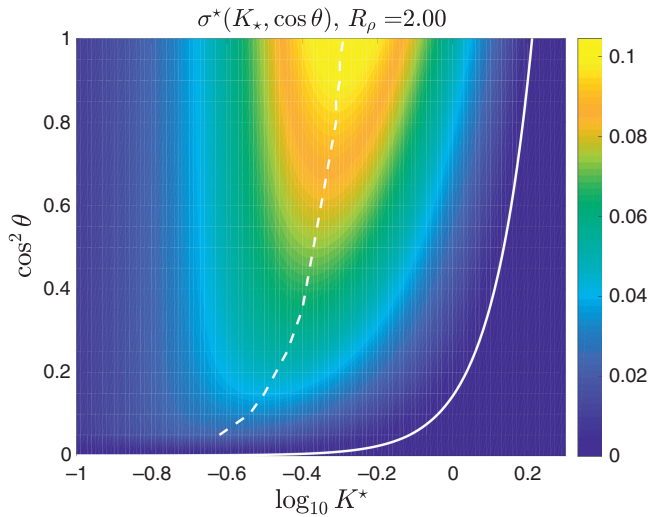
Figure 9.5 Salt fingering growth rate (scaled by $|g\alpha T_z|^{1/2}$) versus wavenumber (scaled by $[|g\alpha T_z|/\kappa_T^2]^{1/4}$) and elevation angle for salt fingering modes with $R_\rho = 2$. Dashed curve: fastest-growing mode for each θ; solid curve: stability boundary.

has a well-defined fastest-growing mode with finite wavenumber (Figure 9.5). As in ordinary convection, the optimal angle of elevation is 90 degrees, i.e., the motions are purely vertical.

Stern (1975) noticed that σ is usually $\ll \nu K^2$ but $\gg \kappa_S K^2$. Accordingly, he simplified (9.7) by replacing $\sigma - \nu K^2$ with νK^2 and $\sigma - \kappa_S K^2$ with σ, reducing the order of the equation to quadratic. The resulting approximation to the fastest-growing mode is

$$\sigma \approx \sqrt{\frac{B_z}{Pr}} \left(\sqrt{\frac{R_\rho}{R_\rho - 1}} - 1 \right) ; \qquad K^4 \approx \frac{B_z}{\kappa_T^2 Pr}. \qquad (9.11)$$

Shown by dashed curves on Figure 9.4, this approximation gives growth rates accurate to within 10 percent when $1.2 < R_\rho < 5$, the most important range for the ocean. Because K is proportional only to the fourth root of B_z, the thickness of salt fingers does not vary by much in the Earth's oceans – it is typically a few centimeters.

Laboratory Experiment

It is easy to produce the salt-finger instability in your kitchen at home, or in the classroom. All that is needed is a glass and spoon, some hot and cold water (about half a glass of each), food coloring, and salt or sugar. First, add the food coloring, and a very slight amount of sugar or salt (usually just a dozen grains or so is enough) to the hot water (about the temperature of a cup of tea), and mix it thoroughly. This will form the warm, salty upper layer. Note that the purpose
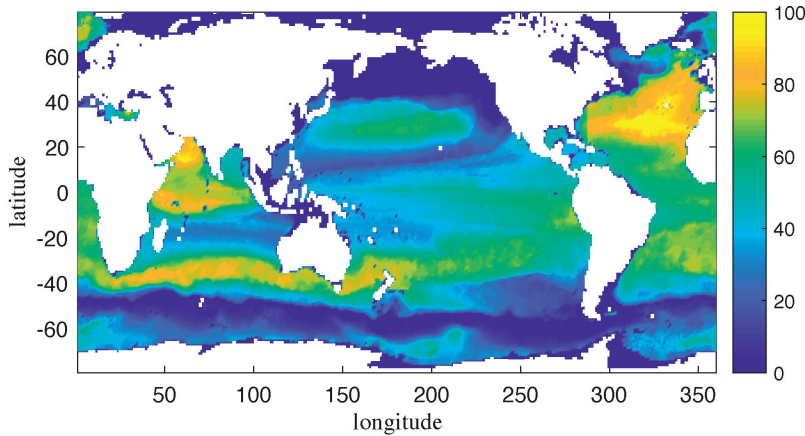
Figure 9.6 Regions of the world's oceans where R_ρ is favorable for salt finger convection. Plotted is the percentage of the uppermost 2000 m in which $1 < R_\rho < 100$. These data were collected and made freely available by the International Argo Program and the national programs that contribute to it. (http://www.argo.ucsd.edu, http://argo.jcommops.org). The Argo Program is part of the Global Ocean Observing System. The BOA-Argo dataset used for this calculation was produced at China Argo Real-time Data Center (Li et al., 2017).

of the food coloring is only to visualize the instability, as in Figure 9.2. It may not be necessary to add the salt or sugar since the food coloring may already have sugar added.

The experiment begins when this colored mixture is added to half a glass of room temperature water from the tap. The most important part of the experiment is to add the warm, salty layer very carefully, so as not to mix too much with the tap water. This is why a spoon is recommended to break the fall of the warm, salty water as it is added. After about a minute, the fingers should form as shown in Figure 9.2.

Geography

The stratification required for the finger regime of double-diffusive convection is found in widespread areas of the subtropical oceans, especially in the Atlantic Ocean and the Mediterranean Sea. The reason is that both surface heating and evaporation are strong, tending to produce warm and salty surface waters. Figure 9.6 shows regions where R_ρ values are low enough for salt fingers to be likely.

9.2.5 Oscillatory Diffusive Convection

We turn now to the stability properties of profiles where both *T* and *S decrease* with height, the opposite situation to salt fingering. This is called the *diffusive* regime of double diffusion, and leads to an instability that is very different from salt fingering.
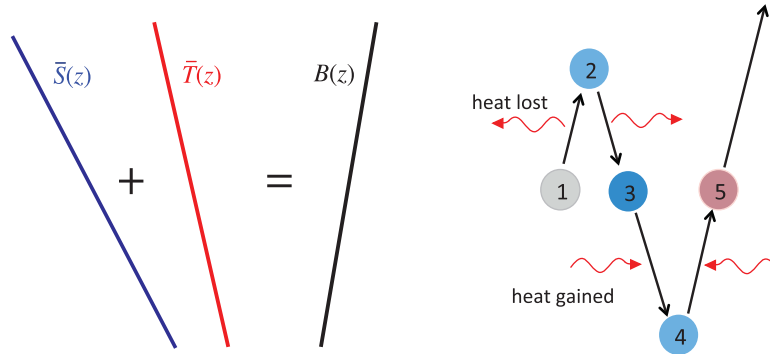
Figure 9.7 Schematic of diffusive convection instability. Cold, fresh water over-
lies warm, salty water, such that the net buoyancy gradient is positive. A water
parcel (1), displaced upward (2), sinks due to buoyancy (3). During this excursion
it loses heat to its surroundings, but not salt, so it now has decreased buoyancy.
The parcel continues downward, becoming lighter than its surroundings (4), then
rises again (5), all the while losing heat. Larger vertical excursions lead to larger
heat exchanges and thus positive feedback.

Referring to Figure 9.7, suppose that a fluid parcel is displaced upward from its
equilibrium position. It will find itself surrounded by fluid that is both cooler and
fresher. Since $\kappa_T \gg \kappa_S$, heat will be transferred from the parcel to the surroundings
much more effectively than salt. The parcel will therefore become denser than its
surroundings and sink. In the warmer environment below, the parcel will lose heat,
but retain its salinity, therefore becoming lighter than its surroundings, after which
it will rise once again. In this way the water parcel performs exponentially growing
oscillations, as our linear stability analysis predicts.

As in salt fingering (and ordinary convection), diffusive convection is most effi-
cient when motions are purely vertical (Figure 9.8). The imaginary part of the
growth rate generally exceeds the real part by an order of magnitude, i.e., the insta-
bility oscillates rapidly but grows slowly. This is true throughout the range of R_ρ
where diffusive convection exists (Figure 9.4).

As per (9.9), the oscillatory mode of double diffusion occurs only over a
restricted range of R_ρ, $0.876 < R_\rho < 1$. Yet, evidence of instability that is
observed in the oceans is seen for a much wider range of R_ρ. A way out of
this conundrum has been suggested by Radko (2016), who found that when even
small amounts of shear are included in the stability analysis of diffusive con-
vection, instability is found over a much larger range of R_ρ. In addition, for
conditions found in the oceans the dominant instability is not, in fact, the oscil-
latory mode described above, but is instead a type of convection that depends on
the action of diffusion on the *mean profiles* of temperature and salinity (described
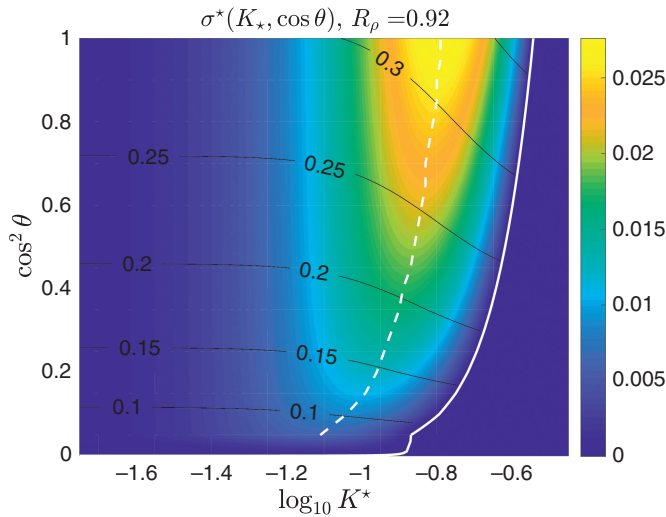below).

Figure 9.8 Scaled growth rates of diffusive convection for $R_\rho = 0.92$. Contours show the imaginary part. Scaling is as in Figure 9.5. Dashed curve: fastest-growing mode for each θ; solid curve: stability boundary.
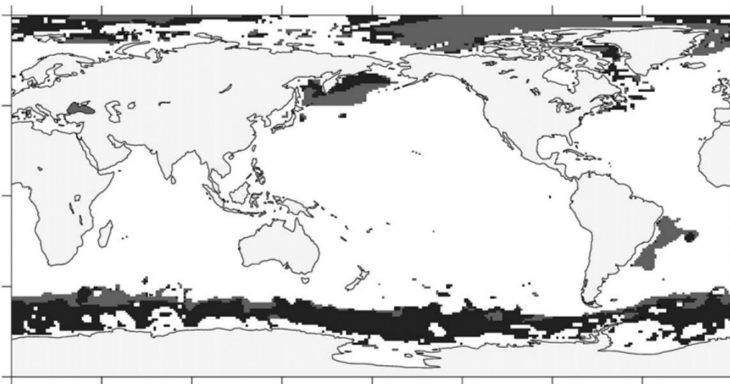

Figure 9.9 Regions of the world oceans where the stratification of the diffusive regime of double diffusion is found with $1/3 < R_\rho < 1$ in dark gray, and $1/10 < R_\rho < 1/3$ in light gray. Reprinted from Kelley et al. (2003), with permission from Elsevier.

Geography

The compound stratification needed for diffusive convection is found most often in the polar regions (Figure 9.9), where ice melt and cold river runoff create a cold, fresh surface layer.

9.2.6 Thermohaline Staircases in Fingering and Diffusive Regimes

If we look more closely at profiles from double diffusive regions, we see that the profiles of T, S, and B are often comprised of a series of mixed layers separated
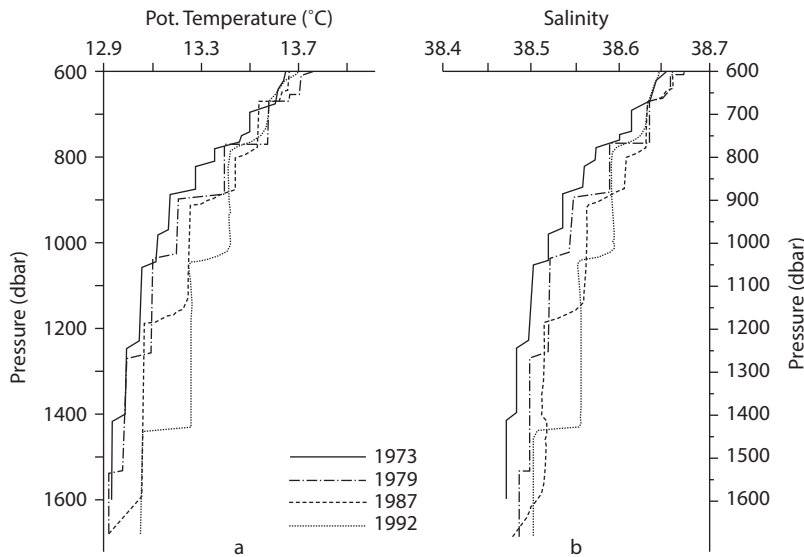
Figure 9.10 Staircase profiles measured in the Tyrrhenian Basin of the Mediterranean Sea over a 19-year period. The vertical axis can be interpreted as depth with 100 dbar roughly 100 m. Reprinted from Zodiatis and Gasparini (1996), with permission from Elsevier.

by sharp interfaces. These so-called thermohaline staircases may occur either in fingering regimes (e.g., the Mediterranean Sea; Figure 9.10) or diffusive regimes (e.g., the Arctic Ocean Figure 9.11). The mechanism of their formation has been a subject of intense discussion since they were first observed in the 1960s and remains so today.

In the diffusive regime, it appears that a convective instability is acting at the edges of each interface. This can be understood by considering the thickening of the $\bar{T}$ and $\bar{S}$ interfaces due to molecular diffusion. Since $\kappa_T > \kappa_S$, the $\bar{T}$ interface tends to become thicker than the $\bar{S}$ interface (Figure 9.12). This results in layers above and below each interface where the gravitationally unstable thermal stratification is not stabilized by salinity. Once the relevant Rayleigh number exceeds the critical value (section 2.4.2), the layers become unstable and produce turbulent convection rolls above and below each interface. The layers are thereby maintained at roughly uniform, but different, temperatures and salinities while the interfaces remain sharp (Carpenter et al., 2012). In the salt fingering regime, staircases may be related to the turbulence-induced instabilities discussed later in section 12.2.

In our discussion of double diffusion we have focused on oceanic observations, but there are many other systems that exhibit double diffusive phenomena. A number of brackish lakes exhibit spectacular thermohaline staircases. The best example is Lake Kivu, located in east Africa on the border between Rwanda and the Democratic Republic of Congo. There, in about 400 m of water, more than
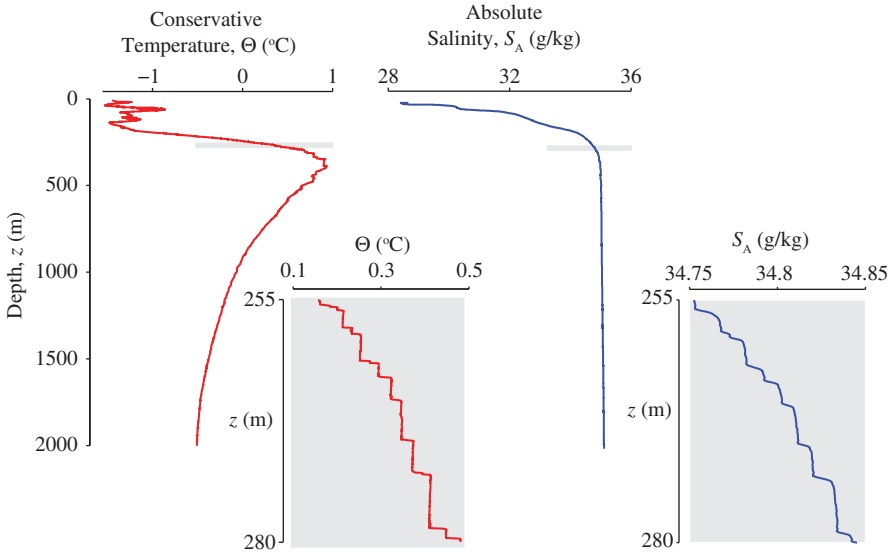
Figure 9.11 Profiles of *T* and *S* from the thermohaline staircase in the Arctic Ocean. The large-scale profiles are shown above, with more detailed plots of the small-scale staircase structure taken from the gray regions. Data for this plot was provided from the Beaufort Gyre Observing System (www.whoi.edu/beaufortgyre/).
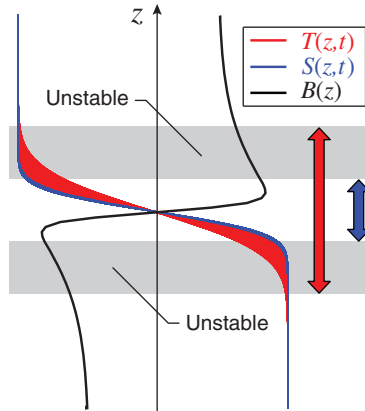

Figure 9.12 Schematic of an interface in a thermohaline staircase of the diffusive regime. Sequential profiles show the thickening of the *T* interface. Arrows represent the final thickness of the *T* and *S* interfaces. The final buoyancy profile is also plotted, with gray regions roughly indicating the gravitationally unstable layers.

300 individual mixed layers can be identified. This diffusive convection system is also interesting in that it has a significant buoyancy contribution from dissolved carbon dioxide and methane gases. In fact, there is so much methane gas present

in the deep waters of Lake Kivu that it is currently being extracted and burned to produce electricity. This extraction is also a safety measure: sudden de-gassing events in smaller lakes have resulted in dense CO_2 gas clouds that suffocated the surrounding inhabitants (Schmid et al., 2004).

Radko (2013) is an excellent source for further information on double diffusive instabilities.

9.3 Bioconvection

The reader may thus far have noticed that instability through convection has a common theme: it is a mechanism that releases the potential energy of a fluid column and converts it to kinetic energy. Normally this potential energy comes from some distribution of a scalar quantity such as temperature, salinity, or water vapor, but more exotic cases can be found. One such case is when the scalar quantity is the concentration of microorganisms. This curious *bioconvection* was noticed by biologists in the laboratory when populations of swimming creatures spontaneously formed hexagonal cell patterns if either the thickness of the fluid layer was large enough, or the concentration of microorganisms was high enough (see Figure 9.13). The potential energy needed for convection exists because (i) the microorganisms are slightly denser than water, and (ii) they instinctively swim upwards in search of sunlight, and are therefore concentrated near the surface.

9.3.1 Equations of Motion

We can understand the onset of bioconvection as a normal mode instability. To this end, we couple the standard Boussinesq equations of motion, reproducing (2.1, 2.3),
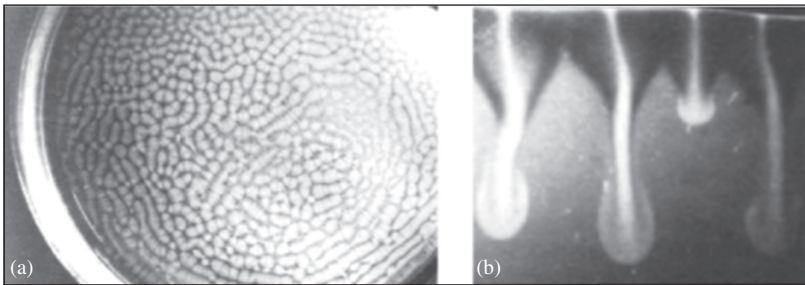

Figure 9.13 Bioconvection in laboratory suspensions of swimming microorganisms. (a) Top view of bioconvection cells in a container of 4 cm diameter and a depth of 6.8 mm. (b) Side view of bioconvection plumes in a deep, narrow container. Photos from Pedley and Kessler (1992), where more information can be found.

$$\vec{\nabla} \cdot \vec{u} = 0 \tag{9.12}$$

$$\frac{D\vec{u}}{Dt} = -\vec{\nabla}\pi + b\hat{e}^{(z)} + \nu\nabla^2\vec{u} \tag{9.13}$$

with an equation that describes the buoyancy in terms of the volumetric concentration of the biota, c, and an equation that describes the evolution of c. We assume that the density of the biota, ρ_1, is a constant slightly greater than the ambient fluid density, ρ_0, which is also assumed to be constant. The total density of the mixture is then given by $\rho = \rho_1 c + \rho_0(1 - c)$, which we can write in terms of buoyancy as

$$b = -\tilde{g}c, \tag{9.14}$$

where $\tilde{g} \equiv g(\rho_1 - \rho_0)/\rho_0$ is referred to as the reduced gravity.

Now let the conservation equation for c take the form

$$\frac{Dc}{Dt} = -\vec{\nabla} \cdot \vec{F}, \tag{9.15}$$

where $\vec{F}$ is a microorganism flux. The flux can be thought to consist of two parts: (i) the flux due to swimming, with speed and direction given by a vector $\vec{V}$, and (ii) the diffusion of c, also due to swimming but on a random trajectory meant to avoid crowds. Thus,

$$\vec{F} = c\vec{V} - \kappa\vec{\nabla}c. \tag{9.16}$$

(In more sophisticated models, the diffusivity is a tensor that incorporates swimming behavior in more detail.) Substituting (9.16) into (9.15) and assuming that the swimming is directed upwards at uniform velocity, $\vec{V} = V_s\hat{e}^{(z)}$, yields a conservation equation for c:

$$\frac{Dc}{Dt} = -V_s c_z + \kappa\nabla^2 c. \tag{9.17}$$

Equations (9.12, 9.13, 9.14) and (9.17) form a complete set. Boundaries are located at $z = -H, 0$, and assumed to be impermeable ($w' = 0$) and either rigid ($w'_z = 0$) or frictionless ($w'_{zz} = 0$). Impermeability also requires that the flux of biota not penetrate the boundaries, viz. $F^{(z)} = 0$.

9.3.2 Equilibrium Solution

We now search for solutions in the form of a motionless equilibrium with small perturbations imposed on it, i.e., $c(\vec{x}, t) = C(z) + \epsilon c'(\vec{x}, t)$, $\vec{u} = \epsilon\vec{u}'$, and $\pi = \Pi(z) + \epsilon\pi'(\vec{x}, t)$. The conservation equation (9.15) requires that $F^{(z)}$ be independent of depth, and since $F^{(z)}$ is zero at the boundaries, it must be zero everywhere. Hence,

$$V_s C_z = \kappa C_{zz} \quad \Rightarrow \quad C(z) = C_0 e^{\frac{V_s}{\kappa} z}, \tag{9.18}$$

where the constant C_0 is the biota density at the surface.

9.3.3 The Perturbation Equations

We now proceed to the order ϵ and look at the evolution of small perturbations. Following the usual steps to eliminate the pressure and the horizontal velocity components (e.g., section 3.1.2), the equations are reduced to:

$$\frac{\partial}{\partial t} \nabla^2 w' = -\tilde{g} \nabla_H^2 c' + \nu \nabla^4 w', \tag{9.19}$$

$$\frac{\partial}{\partial t} c' = -C_z w' - V_s c'_z + \kappa \nabla^2 c'. \tag{9.20}$$

Note that (9.19) and (9.20) are analogous to the perturbation equations for ordinary convection (2.17, 2.18) except for the second term on the right-hand side of (9.20), which arises from the microorganisms' swimming. A second important difference is that the coefficient C_z is not constant but rather depends on z, necessitating a numerical solution.

We now make the usual normal mode assumption $w' = W_r$; $W = \hat{w}(z)e^{\sigma t + \iota(kx+\ell y)}$ and similar for c', leading to

$$\sigma \nabla^2 \hat{w} = \tilde{g}\tilde{k}^2 \hat{c} + \nu \nabla^4 \hat{w} \tag{9.21}$$

$$\sigma \hat{c} = -C_z \hat{w} - V_s \hat{c}_z + \kappa \nabla^2 \hat{c}, \tag{9.22}$$

where $\nabla^2 = d^2/dz^2 - \tilde{k}^2$. together with

$$C_z = C_0 \frac{V_s}{\kappa} \exp\left(\frac{V_s}{\kappa} z\right) \tag{9.23}$$

and the boundary conditions

$$\hat{w} = 0 ; \quad \hat{c}_z = \frac{V_s}{\kappa} \hat{c} \quad \text{on } z = -H, 0.$$

In the usual fashion, this is all expressed as a generalized eigenvalue problem and solved using the numerical methods developed in previous chapters. The resulting solution may be written as

$$[\sigma, \hat{w}, \hat{c}] = \mathcal{F}(z, \tilde{g}, \tilde{k}, \nu, \kappa, C_0, V_s, H).$$

9.3.4 Scaling

It is convenient to scale the problem using the length H, the time H^2/κ, and the concentration C_0, resulting in

$$\sigma_\star \nabla_\star^2 \hat{w}^\star = Ra \; Pr \; \tilde{k}_\star^2 \hat{c}^\star + Pr \; \nabla_\star^4 \hat{w}^\star \qquad (9.24)$$

$$\sigma_\star \hat{c}^\star = -\lambda \exp(\lambda z^\star) \hat{w}^\star - \hat{c}_{z^\star}^\star + \nabla_\star^2 \hat{c}^\star, \qquad (9.25)$$

with boundary conditions

$$\hat{w}^\star = 0, \;\; \hat{c}_{z^\star}^\star = \lambda \hat{c}^\star, \;\; \text{and either } \hat{w}_{z^\star}^\star = 0 \;\; \text{or} \;\; \hat{w}_{z^\star z^\star}^\star = 0$$

on $z^\star = -1, 0$. The quantity Ra appearing in (9.24) plays a role similar to the Rayleigh number in ordinary convection, and is defined as

$$Ra = \frac{\tilde{g} C_0 H^3}{\kappa \nu}.$$

The parameter Pr is not the usual Prandtl number; it is the ratio of the viscosity of the water to the diffusivity of the biota. The analogy is close, though, since it is the biota that determine the buoyancy via (9.14). A typical value for Pr is 2 (see below). The parameter λ can be thought of as a nondimensional ratio of the swimming flux to the diffusive flux:

$$\lambda = \frac{V_z H}{\kappa}.$$

The solution procedure is now

$$[\sigma_\star, \hat{w}_\star, \hat{c}^\star] = \mathcal{F}(z^\star, RaPr, \tilde{k}_\star, Pr, 1, 1, \lambda, 1),$$

i.e., the solution is determined by the horizontal wavenumber $\tilde{k}^\star$ and the parameters Ra, Pr, and λ. As in ordinary convection, the direction of the wave-vector (k, ℓ) is immaterial.

9.3.5 The Stability Boundary

Figure 9.14 shows the (purely real) growth rate as a function of $k^\star$ and Ra for the particular case $Pr = 2$, $\lambda = 3$. The bottom boundary is rigid; the top is frictionless (to mimic a lab experiment). As in the Rayleigh-Benard problem, there is for each wavenumber a critical value of Ra, Ra_c, above which $\sigma^\star = 0$ grows monotonically from zero. The minimum critical Rayleigh number for this case is 488, occurring at $k_\star = 1.54$. For every $Ra > Ra_c$, there is a unique fastest-growing mode which occurs at monotonically growing wavenumbers.

On the stability boundary of a stationary mode, $\sigma^\star = 0$, so that the left-hand sides of (9.24) and (9.25) vanish. If we then divide (9.24) by Pr, Pr is removed from the problem. This tells us that both the critical Rayleigh number and the wavenumber at which it occurs are independent of Pr, as in Rayleigh-Benard convection (section 2.4.2). However, both parameters depend on the flux ratio λ as shown in Figures 9.15(a,b), respectively.

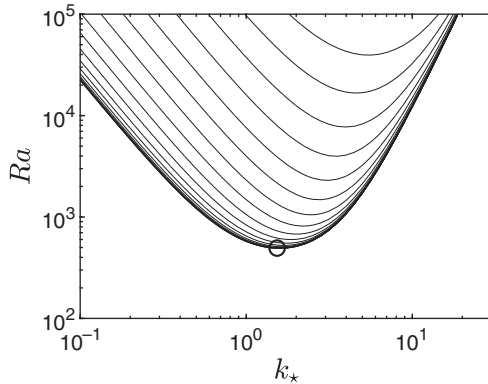You can explore bioconvection further yourself in project B.3.

Figure 9.14 Scaled growth rate of bioconvection versus wavenumber and Rayleigh number. The circle indicates the critical state. Logarithmic contour spacing represents a factor of 1.8; maximum growth rate is 291.
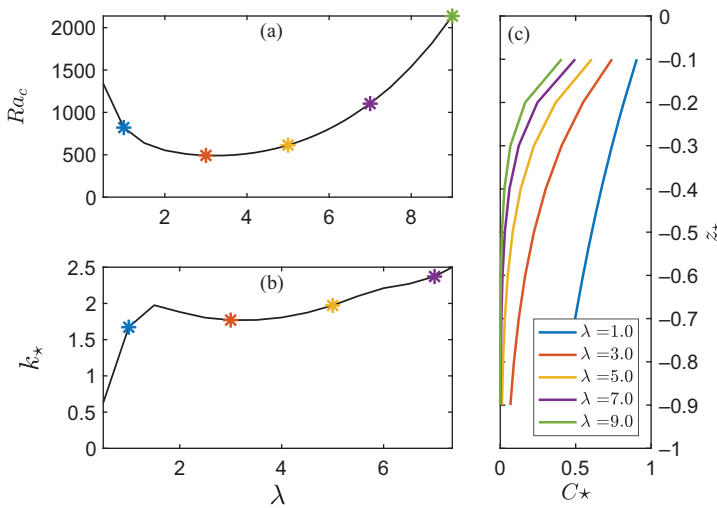

Figure 9.15 Critical values of the Rayleigh number (a) and the corresponding scaled wavenumber (b) as functions of λ. (c) Equilibrium concentration profiles for selected λ, color-coded to match (a) and (b).

9.4 CO₂ Sequestration

The burning of fossil fuels for energy production has led to a potentially harmful increase in the concentration of carbon dioxide gas in the atmosphere (CO_2 is a byproduct of the reaction). One of the techniques proposed to combat this increase is to store CO_2 in deep (around $800 - 3{,}000$ m) underground aquifers. The aquifers consist of a porous rock medium that is filled with saline groundwater, and
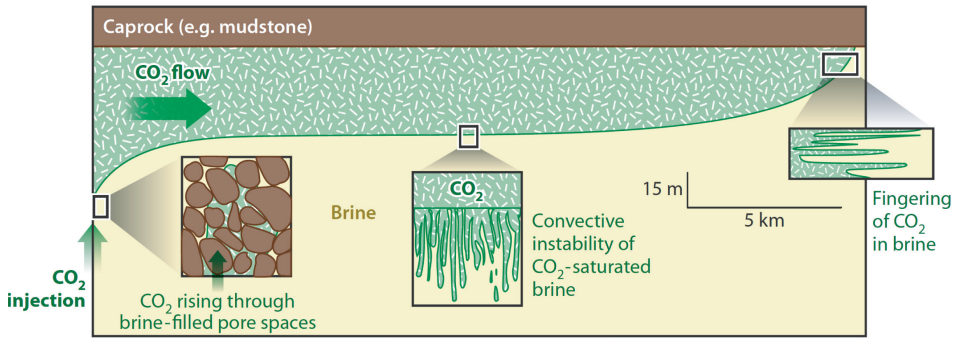
Figure 9.16 Injection and flow of liquid CO_2 along a capping rock in a saline underground aquifer (Huppert and Neufeld, 2014).
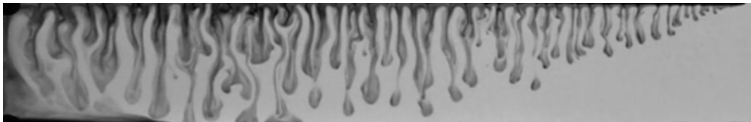

Figure 9.17 Laboratory experiment performed to study the instability of buoyant CO_2 current (dark colors). Analog fluids are water (which takes the role of the CO_2) and propylene glycol (which takes the role of the groundwater). The dark CO_2-like fluid was injected on the left and sheds convective plumes as it propagates to the right along the top of the photo [see MacMinn and Juanes (2013) for more details]. Photo courtesy of Christopher MacMinn.

is capped above by an impermeable layer that is usually gently sloping. The idea is to inject CO_2 into the porous medium below the capping layer where it will be stored. Since the liquid CO_2 at these pressures and temperatures is more buoyant than the saline groundwater, it will rise to the capping rock and spread laterally (Figure 9.16). It is possible for the CO_2 to flow laterally for tens or hundreds of kilometers, whence it may escape the coverage of the capping rock and find its way back to the atmosphere. However, there are ways of trapping the CO_2, one of which consists of dissolving it into the underlying groundwater.

This dissolution and trapping of the CO_2 into the ambient groundwater is aided by a convection-type instability that arises due to the equation of state. Despite the liquid CO_2 being more buoyant than the ambient water, the *mixture* of CO_2 and water is actually denser than either of the two fluids when pure. This has the effect of creating a negatively buoyant layer at the interface of the two fluids that can become unstable when conditions are right. The situation is similar to that described for the maintenance of thermohaline staircases in the diffusive regime (see the end of section 9.2.5, and Figure 9.12). The instability can be seen in the laboratory experiment shown in Figure 9.17, where the buoyant gravity current

forms convective plumes as it propagates from left to right along the top boundary. It is important to understand the increased dissolution of CO$_2$ that is caused by this instability, as it is an important mechanism in setting the possible travel distance of the current, as well as influencing the amount of CO$_2$ that is trapped in the aquifer.